Pore-network analysis of two-phase water transport in gas diffusion layers of polymer electrolyte membrane fuel cells

3 AUTHORS, INCLUDING:

Jin Hyun Nam
Daegu University

56 PUBLICATIONS **1,300** CITATIONS

SEE PROFILE

Pore-network analysis of two-phase water transport in gas diffusion layers of polymer electrolyte membrane fuel cells

Kyu-Jin Lee [a], Jin Hyun Nam [b,*], Charn-Jung Kim [a]

[a] School of Mechanical and Aerospace Engineering, Seoul National University, Seoul 151-742, Republic of Korea
[b] School of Mechanical and Automotive Engineering, Kookmin University, 861-1 Jeongneung-dong, Seongbuk-gu, Seoul 136-702, Republic of Korea

ABSTRACT

A pore-network model was developed to study the water transport in hydrophobic gas diffusion layers (GDLs) of polymer electrolyte membrane fuel cells (PEMFCs). The pore structure of GDL materials was modeled as a regular cubic network of pores connected by throats. The governing equations for the two-phase flow in the pore-network were obtained by considering the capillary pressure in the pores, and the entry pressure and viscous pressure drop through the throats. Numerical results showed that the saturation distribution in GDLs maintained a concave shape, indicating the water transport in GDLs was strongly influenced by capillary processes. Parametric studies were also conducted to examine the effects of several geometrical and capillary properties of GDLs on the water transport behavior and the saturation distribution. The proper inlet boundary condition for the liquid water entering GDLs was discussed along with its effects on the saturation distribution.

1. Introduction

Liquid water is one of the crucial factors that limit the power and efficiency of polymer electrolyte membrane fuel cells (PEMFCs) [1]. Water is continuously produced by electrochemical reactions during the operation of PEMFCs. If the product water is not properly removed from PEMFCs, it condenses in electrodes and subsequently floods the pores in gas diffusion layers (GDLs) or blocks the reactant flow in gas channels (GCs). The liquid water present in PEMFCs hinders effective diffusion of fuel and oxidant gases towards catalyst layers (CLs), resulting in a reduced catalyst effectiveness or a slow dynamic response. Moreover, the volume expansion of liquid water upon freezing may lead to a mechanical failure when PEMFCs are exposed to sub-zero temperature conditions. Therefore, the transport of liquid water in PEMFCs has been an important topic of recent researches.

Conventionally, studies on the water transport through polymer electrolyte membranes (PEMs) by electro-osmosis, back-diffusion and hydraulic permeation processes have been conducted in the context of the water management in PEMFCs. Currently, efforts are being directed to develop more efficient PEMFCs which can operate at higher power densities with higher water production rates. This

requires more knowledge about the water transport and flooding behaviors in GCs and GDLs. Accordingly, many works have been reported concerning the water transport in GCs, including experimental observations of the transport behavior of water droplets in GCs of transparent PEMFCs [2–6] as well as numerical simulations of the behavior based on volume of fluid (VOF) methods utilizing computational fluid dynamics (CFD) tools [7–9].

The transparent PEMFCs provided a straightforward way to observe an important characteristic of GDLs, i.e., the breakthrough of liquid water from a GDL to a GC. However, it is still difficult to observe the transport behavior of liquid water and to measure its saturation distribution inside very thin GDLs. Thus, only few experimental studies have so far been reported on the transport behavior and the saturation distribution in GDLs. Nam and Kaviany [10] reported the microscale behavior of vapor condensation and liquid water transport in a hydrophobic GDL observed by an environmental scanning electron microscope (ESEM). The ESEM technique was also used to observe the microscale behavior of water droplets in hydrophobic CL [11,12]. Recently, Litster et al. [13] and Djilali [14] conducted microscopic observations of the transient water transport behavior inside a GDL using a fluorescein dye solution.

Several researchers reported the water saturation levels in GDLs which were indirectly evaluated by measuring the pressure drop or the concentration loss in PEMFCs [15–17]. Although the data are dependent on the liquid water content in PEMFCs, the transformation of them into the saturation levels produces uncertainty.

Recently, neutron radiographic techniques have been employed in the direct measurement of liquid water content in operating PEMFCs [18,19]. The neutron radiographic techniques provided the thickness-wise averaged water content in GDLs or in PEMFCs but could not resolve the variation of water content along the small thickness of GDLs. Theoretical modeling can provide a way to study the water transport phenomena in GDLs while avoiding the experimental difficulties.

The water transport in GDLs has been predicted by continuum two-phase flow models based on macroscopic two-phase properties, such as the capillary pressure versus saturation correlation, so called the P_c–S curve, and the relative phase permeability $K_{rl}(S)$ as a function of saturation S. The Leverett J-function $J(S)$ has been widely used to correlate the capillary pressure and the liquid water saturation in hydrophobic GDLs [20–28]. The continuum models generally predict that the steady saturation distribution in GDLs have a convex shape along the flow direction. Although accepted as a standard model, whether the continuum two-phase flow models properly describe the water transport phenomena in GDLs or not is still uncertain. None of the researchers were able to prove the validity of the continuum models primarily due to the lack of experimental results regarding the steady and transient saturation distributions inside GDLs.

More fundamental models are currently required to fully understand the transport behavior of liquid water in hydrophobic GDLs of PEMFCs. In this sense, a pore-network model can be a useful analysis tool. In fact, several studies have been published recently on the pore-network modeling of the water transport in GDLs. Markicevic et al. [29], and Gostick et al. [30] conducted pore-network studies to numerically determine the relative phase permeabilities and the macroscopic P_c–S curves of GDLs. But they did not provide the saturation distribution in GDLs during the operation of PEMFCs. On the other hand, Sinha and Wang [31] obtained the transient saturation distribution in a GDL through a dynamic pore-network simulation, and showed that the invasion percolation process might be an important water transport mechanism.

In this study, a new pore-network model for the water transport in hydrophobic GDLs was developed. Regular cubic networks composed of pores and pore-connecting throats were generated to imitate the pore structure of fibrous GDL materials. The microscale two-phase flow in the pore-networks was formulated based on the pore-level (microscopic) capillary pressure in pores, and the entry pressure and viscous flow conductance in throats. And the conservation equations were solved for both (liquid phase) water and (gas phase) air. The pore-network model was used then for the detailed investigation of the transport behavior and the saturation distribution of liquid water in the full thicknesses of GDLs during the operation of PEMFCs. The effects of several geometrical and capillary properties of GDLs were also studied parametrically.

2. Theory and calculation

Liquid water in hydrophobic porous media does not wet the surface since more energy is required for wetting. Thus, it exists preferentially as liquid droplets or blobs and resides in larger pores as shown in Fig. 1(b) to reduce the contact area with hydrophobic surfaces. This is exactly opposite to the liquid water behavior in hydrophilic porous media, i.e., the formation of liquid films preferentially residing in smaller pores as shown in Fig. 1(a). The capillary pressure P_c is defined as the pressure difference across the interface, or the pressure difference between (gas phase) air P_a and (liquid phase) water P_w [32]

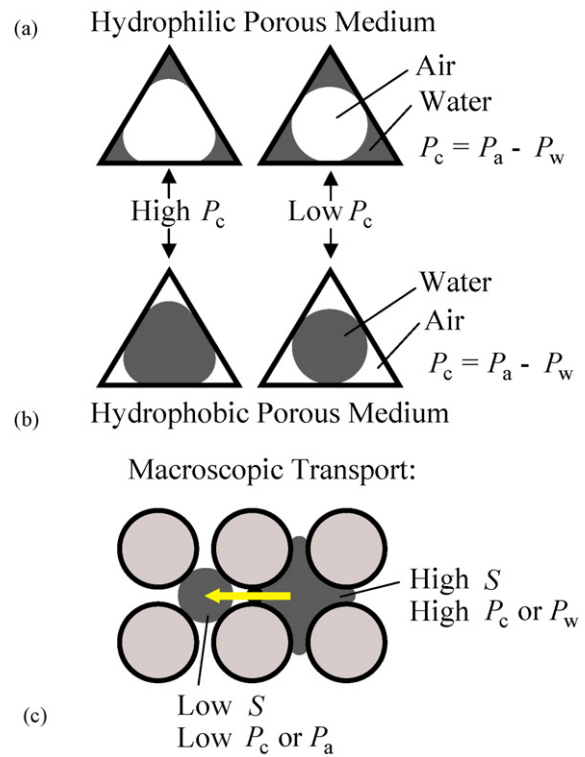$$P_c = P_g - P_l = P_a - P_w. \tag{1}$$

Fig. 1. The microscopic configuration of liquid water in (a) hydrophilic and (b) hydrophobic porous media, and (c) the macroscopic water transport due to a saturation gradient.

Eq. (1) reduces to $P_c = -P_w$ when the gauge pressure of air is rather constant around zero. This situation is normally encountered in PEMFC operations. Thus, the magnitudes of the capillary pressure and the gauge pressure of liquid water are generally equal in GDLs.

The capillary pressure in porous media is governed by the interfacial curvature between the two phases. According to Laplace–Young equation, the capillary pressure is

$$P_c = \sigma \cos \theta_w \left(\frac{1}{R_1} + \frac{1}{R_2} \right) = \frac{2\sigma \cos \theta_w}{r_{w/a}}, \tag{2}$$

where σ is the surface tension, θ_w is the contact angle of water, R_1 and R_2 are the principal radii of curvature, and $r_{w/a}$ is the mean radius of curvature of the water/air interface. Note that the capillary pressure is negative ($P_w > P_a$) for hydrophobic GDL materials as their contact angle is larger than 90° ($\theta_w \approx 120°$).

From a macroscopic viewpoint, the capillary pressure in porous media can be expressed as a function of the wetting (also non-wetting) phase saturation. This is because the curvature of the liquid/gas interface generally increases with the volume content of the non-wetting phase due to the limited pore space available. The Leverett J-function $J(S)$ is a typical example of such an approach, correlating the macroscopic capillary pressure and the phase saturation in porous media. For hydrophobic GDLs, the Leverett J-function can be expressed in terms of the water saturation S_w [32]

$$J(S_w) = \frac{P_c (K/\varepsilon)^{1/2}}{\sigma \cos \theta_w}, \tag{3}$$

where K is the absolute permeability and ε is the porosity. Note that $J(S_w)$ is a monotonic increasing function of the water saturation, and thus the pressure of liquid water increases with S_w. Thus, the macroscopic transport of liquid water occurs from a higher saturation region towards a lower saturation region as shown in Fig. 1(c). A
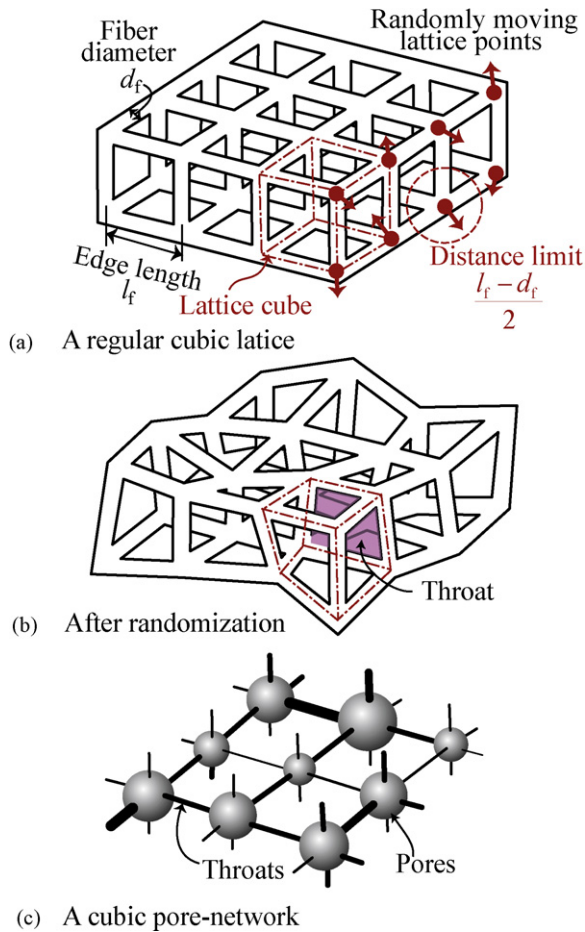
Fig. 2. The generation of a pore-network: a layer of a cubic fiber lattice (a) before and (b) after a randomization procedure, and (c) a resulting cubic network of pores connected by throats.

more comprehensive explanation on the water transport behaviors in hydrophobic GDLs may be found in Nam and Kaviany [10].

2.1. Pore-network generation

The carbon papers or clothes with PTFE coating are generally used as GDLs in PEMFCs. The fibrous solid structure of GDL materials was modeled as a randomized three-dimensional (3D) cubic lattice comprised of short overlapping cylindrical rods located along the edges of the lattice. Fig. 2(a) shows a layer of a cubic fiber lattice with a fiber diameter d_f and a uniform edge length l_f. In order to simulate the random nature of GDL materials, the lattice points were moved in random directions within a distance limit of $(l_f - d_f)/2$ as shown in Fig. 2(b). Then, the remaining void space in the exterior of the cylindrical rods was used to define a pore-network.

A pore in the fiber lattice is illustrated as a dash-dotted cube (a lattice cube) in Fig. 2(b) and a throat is illustrated as a shaded face of the cube. The pore volume V_p was obtained by subtracting the volume of fibers in the pore from the volume of the lattice cube. And the throat area A_t was defined as the smallest opening area of the corresponding face. It should be noted that throats were treated as volumeless passages in the present model by assigning all void volume to pores. However, in the evaluation of the viscous flow resistances through throats, the passage length of throats l_t was assumed to be equal to the fiber diameter d_f. Each pore in the fiber lattice had six quadrilateral throats, and thus could communicate with six adjacent pores through each corresponding throat. This

topological structure (the coordination number Z of 6) resulted in a regular cubic network composed of pores connected by throats, as shown in Fig. 2(c).

The pore structure of GDL materials is generally anisotropic due to their fibrous nature. However, pore-networks were generated to have a rather isotropic pore structure by using a constant fiber diameter d_f of 10 μm and a uniform edge length l_f of 20 μm in generating the initial cubic fiber lattices. This was partly because of the lack of available data on the pore size distributions of GDL materials in different directions. However, the use of isotropic pore-networks may be justified by the fact that the degree of anisotropy of GDL materials measured by directional (in-plane and through-plane) permeabilities or diffusivities was reported to be small [33,34].

The geometrical parameters for the pore-networks used in the present study are summarized in Table 1. The domain size of the pore-networks was chosen to be $20 \times 20 \times 10$ after a grid dependence test, which corresponded roughly to the physical dimension of 400 μm × 400 μm × 200 μm in the x-, y- and z-directions (see Section 2.3 for the definition of the coordinates). The mean porosity ε was estimated to be about 0.73.

2.2. Two-phase flow equations

2.2.1. Throat entry pressure

Fig. 3(a) depicts a liquid water droplet invading into a pore through a throat in hydrophobic GDL materials. In order to fit into the small throat, liquid water should reduce the mean radius of curvature of the water/air interface $r_{w/a}$ by having a sufficiently high pressure. The minimum (magnitude) capillary pressure for a non-wetting fluid to penetrate into a throat is called as the throat entry pressure P_t and this is a function of the geometry and capillary properties of the throat. In this study, the hydraulic radius r_t was assumed to be equal to the largest radius of curvature $r_{w/a}$ required for liquid water to invade into a hydrophobic throat. Then, the throat entry pressure was calculated similar to Eq. (2) as

$$P_t = \frac{2\sigma \cos\theta_w}{r_t}. \tag{4}$$

Note that the throat entry pressures of rectangular throats are exactly determined by using the hydraulic radius.

2.2.2. Flow conductance

The viscous flow through throats was formulated based on the Poiseuille law [35]. The volumetric flow rate $Q_{i \to j}$ from a pore i to a

Table 1
Physical parameters for the pore-network analysis

| Parameter	Explanation	Value
d_f	Fiber diameter	10 μm
l_f	Edge length of fiber lattice	20 μm
L_z^0	GDL thickness	200 μm
$\bar{r}_t$	Mean throats radius (hydraulic radius)	4.77 μm
Σ_{r_t}	Standard deviation of throat radius	0.54 μm
$\bar{V}_p$	Mean pore volume	5596 μm³
θ_w	Contact angle of water	120°
ε	Mean porosity	0.73
γ	Compression ratio	1.0
f	Pore distortion factor	0.5
I	Current density	1.0 A/cm²
σ	Surface tension	0.0679 N/m
μ_a	Viscosity of air	1.95×10^{-5} Pa s
μ_w	Viscosity of water	58.4×10^{-5} Pa s
$N_x \times N_y \times N_z$	Size of calculation domain	$20 \times 20 \times 10$
$\bar{L}_x \times \bar{L}_y \times \bar{L}_z$	Mean dimension of calculation domain	400 μm × 400 μm × 200 μm
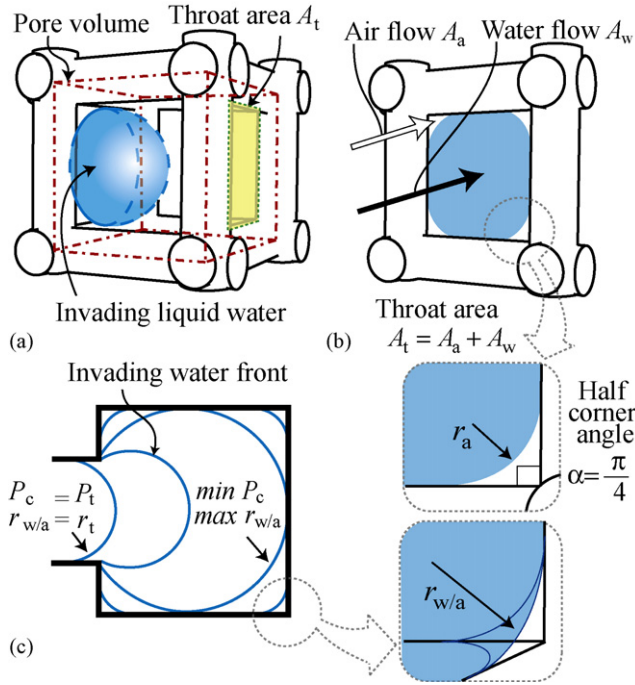
Fig. 3. The microscale behaviors of liquid water in a hydrophobic pore-network: (a) the invasion of liquid water into a pore, (b) the two-phase water/air flow through a throat, and (c) the microscopic behavior of a liquid water droplet in a cubic pore.

neighboring pore j through a throat is proportional to the pressure drop $(P_i - P_j)$ across the throat as

$$Q_{i \rightarrow j} = G_{ij}(P_i - P_j). \tag{5}$$

The air conductance G_a^I for the single-phase flow through throats was determined as

$$G_a^I = \frac{A_t r_t^2}{8\mu_a l_t}, \tag{6}$$

where A_t is the throat area, μ_a is the viscosity of air, and l_t is the passage length of throats. The superscript I in Eq. (6) denotes the single-phase flow. The passage length of throats l_t was assumed to be equal to the fiber diameter d_f ($l_t = d_f$) in order to properly evaluate the flow resistance exerted by the fibrous solid structure in GDL materials. Note that the hydraulic radius r_t in Eq. (6) is naturally suited as a length scale for determining the viscous resistance of quadrilateral throats.

When water/air two-phase flow occurs through a hydrophobic throat, the wetting phase (air) flows along the corners of the throat and the non-wetting phase (water) passes through the center, as shown in Fig. 3(b). The flow area for air in four corners of the rectangular throat was calculated as [36]

$$A_a = 4r_a^2 \tan\alpha \left[\frac{\cos\theta_a}{\sin\alpha}\cos(\alpha + \theta_a) - \left(\frac{\pi}{2} - (\alpha + \theta_a)\right) \right], \tag{7}$$

where θ_a is the contact angle of air ($\theta_a = \pi - \theta_w$) and α is the half angle of the corners (set to be $\pi/4$ for rectangular throats). The arc radius r_a of the water/air interface in the throat in Eq. (7) was determined as

$$r_a = \frac{\sigma\cos\theta_w}{P_c^{up}} \tag{8}$$

where P_c^{up} denotes the capillary pressure in the upstream pore ($P_c^{up} > P_t$). Note that Eq. (8) can be derived from Eq. (2) by setting

one radius of curvature to be infinite ($R_2 \rightarrow \infty$). Then, the flow area for water was calculated as

$$A_w = A_t - A_a. \tag{9}$$

The water conductance G_w^{II} for the two-phase flow through throats was calculated as

$$G_w^{II} = \frac{A_w r_t^2}{8\mu_w l_t}, \tag{10}$$

where μ_w is the viscosity of water and the superscript II denotes the two-phase flow. Likewise, the air conductance G_a^{II} for the two-phase flow through throats was obtained as

$$G_a^{II} = \frac{A_a r_a^2}{\beta\mu_a l_t}, \tag{11}$$

where β is a dimensionless resistance factor [37–39]. See the appendix for the physical meaning and the full expression of β.

2.2.3. Pore-level capillary pressure

The capillary pressure in a pore is determined by the curvature of the water/air interface formed inside the pore. This interfacial curvature is known to be affected by various factors such as the pore structure, local saturation, contact angle, hysteresis, etc. However, considering all the factors for all randomly deformed pores in a pore-network is impractical, not to mention computationally expensive. Thus, the water/air interface inside each pore was assumed quasi-static, by neglecting the hysteresis effect. And it was also assumed that the capillary pressure behavior in pores could be properly represented by the pore-level P_c–S curves derived for cubic pores according to [35] as shown in Fig. 3(c).

Fig. 4 shows the pore-level P_c–S curves used in the present study. The initial decreasing parts of the P_c–S curves were obtained by considering the capillary pressure of an expanding spherical water droplet in hydrophobic media shown in Fig. 3(c). That is

$$P_c(S_w) = 2\sigma\cos\theta_w\left(\frac{1}{r_s}\right) = 2\sigma\cos\theta_w\left(\frac{3}{4\pi}V_p S_w\right)^{-1/3}, \tag{12}$$

where r_s is the sphere radius and V_p is the pore volume. Note that the sphere radius r_s is the same as the mean radius of curvature of the water/air interface $r_{w/a}$ until the water droplet touches the hydrophobic surface. Thus, the sphere radius r_s increases according to the water saturation S_w, leading to the decrease in the capillary pressure in magnitude. As shown in Fig. 4, this trend continues until the capillary pressure reaches its local minimum at $S_w = S_{tr}$. The transition saturation S_{tr} is defined as the ratio of the volume of the inscribed sphere (whose radius is r_{max}) to the pore volume V_p as

$$S_{tr} = \frac{4\pi}{3}\frac{r_{max}^3}{V_p}. \tag{13}$$

After the transition saturation, the capillary pressure starts to increase rather steeply and eventually approaches infinity as $S_w \rightarrow 1$, as shown in Fig. 4. It is difficult to determine the exact functional form for the increasing parts of the P_c–S curves. Thus, an approximate functional form was developed by considering the configuration of a liquid water droplet in a cubic pore as shown in Fig. 3(c). If the mean radius of curvature of the water/air interface $r_{w/a}$ is uniform in the cubic pore, the air volume residing in eight corners becomes proportional to $r_{w/a}^3$. In this case, the capillary pressure and the saturation can be correlated as

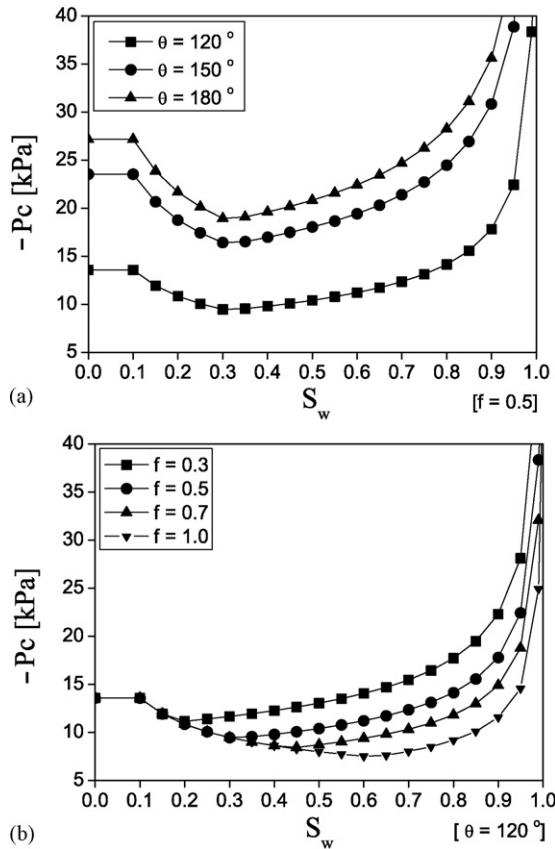$$P_c(S_w) = 2\sigma\cos\theta_w[aV_p(1 - S_w)]^{-1/3}. \tag{14}$$

Fig. 4. The variation of pore-level (microscopic) capillary pressure curves with respect to (a) the pore distortion factor f and (b) the contact angle θ_w.

Here a is a parameter to match the capillary pressures of Eq. (12) and Eq. (14) at the transition saturation $S_w = S_{tr}$

$$a = \frac{3}{4\pi}\left(\frac{S_{tr}}{1-S_{tr}}\right). \tag{15}$$

The undistorted pores have the largest inscribed sphere radius $r_{max,c}$ and the largest transition saturation $S_{tr,c}$ of about 0.6. However, most pores in the simulated pore-networks became distorted after the randomization procedure, which resulted in smaller r_{max} and S_{tr}. This situation was considered by introducing the pore distortion factor f which was defined as the ratio of the inscribed sphere volume in the distorted pores $(4\pi/3)r_{max}^3$ to that in the undistorted cubic pores $(4\pi/3)r_{max,c}^3$ $(0 < f \le 1)$. Reducing f results in a smaller transition saturation and thus a higher capillary pressure at the same saturation, as shown in Fig. 4(a). The effect of the contact angle θ_w on the pore-level P_c–S curves is also shown in Fig. 4(b), where larger contact angle increases the capillary pressure level but does not change the general trend of the curves. In this study, a constant f of 0.5 was assumed despite the pore distortion factors for all pores in GDLs are random in nature. Instead, the impact of variable pore distortion factors on the water transport was discussed along with the parametric results for f. The contact angle θ_w was assumed to be 120°.

2.2.4. Conservation equations
The volume conservation equation for each phase in a pore i is written as

$$\frac{V_{p,i}}{\Delta t}(S_{w,i} - S_{w,i}^o) + \sum_j G_{w,ij}^o(P_{w,i} - P_{w,j}) = 0 \quad \text{for water,} \tag{16a}$$

$$\frac{V_{p,i}}{\Delta t}(S_{a,i} - S_{a,i}^o) + \sum_j G_{a,ij}^o(P_{a,i} - P_{a,j}) = 0 \quad \text{for air,} \tag{16b}$$

where j denotes the six neighboring pores of the pore i and the superscript o denotes the previous time step.

The above equations link the rate of change of phase saturation in a pore to the sum of phase flow rate from its neighboring pores. Note that Eqs. (16a) and (16b) are highly non-linear due to the presence of two phases. To assure the stability of the solution procedure, the flow conductances $G_{w,ij}$ and $G_{a,ij}$ were determined based on the water saturation obtained at the previous time step. This approach is similar to the implicit in pressure and explicit in saturation (IMPES) scheme used in the reservoir simulation [40].

Adding Eqs. (16a) and (16b), and using $S_w + S_a = 1$ and $P_c = P_a - P_w$ results in a single equation for the air pressure

$$\sum_j [(G_{a,ij}^o + G_{w,ij}^o)(P_{a,i} - P_{a,j}) - G_{w,ij}^o(P_{c,i}^o + P_{c,j}^o)] = 0 \tag{17}$$

and this equation was solved iteratively for each time step.

2.3. Initial and boundary conditions

Pore-networks were considered to be infinite in the x- and y-directions by using a periodic boundary condition as shown in Fig. 5. It was assumed that the pore-networks were initially filled with air and then liquid water was introduced through an inlet surface at a constant flow rate Q_{inj}. It was also assumed that the injection flow rate was uniformly distributed over the inlet surface, leading to a uniform inlet flux condition with Q_{inj}/A_z. In the calculation, a constant generation of liquid water by the amount of $Q_{inj}/(N_x N_y)$ was imposed to all the pores contacting the inlet surface.

At an outlet surface, a constant air pressure of 1 atm was applied as shown in Fig. 5. When the calculated flow rate exiting through the outlet surface became higher than 99% of the injection flow rate Q_{inj}, the water transport in the pore-networks was considered to reach a steady state. Further calculation resulted in no noticeable change in the saturation distribution.

2.4. Numerical procedure

A simulation was started with the generation of a pore-network and the subsequent pre-calculation of the pore volume V_p, the throat area A_t, the throat entry pressure P_t, etc. During the transient
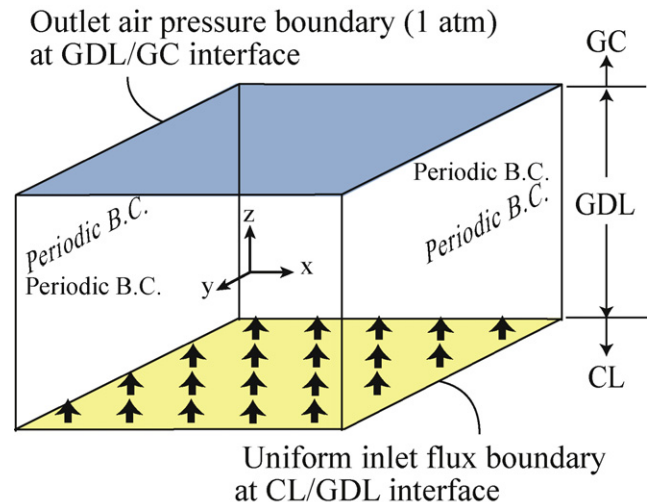

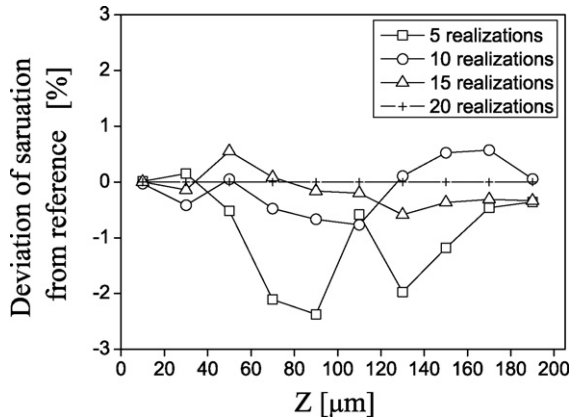**Fig. 5.** The initial and boundary conditions for the pore-network analysis.

Fig. 6. The convergence of the average saturation distribution with respect to the number of simulated pore-network realizations.

calculation, Eq. (17) was solved first to obtain the air pressure P_a, which was then added to $-P_c^o$ to update the liquid water pressure as $P_w = P_a - P_c^o$. The next step was to update the water saturation S_w by integrating Eq. (16a) based on the obtained P_w. Finally, the capillary pressure P_c was updated based on Eq. (12) or Eq. (14) according to the obtained S_w. This numerical procedure was repeated for the next time step and was continued until the steady state criterion was met. In the present study, small time steps less than 10^{-4} s were used to ensure the stability of the numerical solution.

3. Results

3.1. Water transport behavior

Numerical analysis of the water transport in hydrophobic GDLs requires statistical averaging due to the stochastic nature of the phenomena. Fig. 6 shows the average saturation distributions obtained using different numbers of pore-network realizations. It is observed that 10 pore-network realizations are sufficient to obtain a converged saturation distribution within ±1% variation. According to the convergence test result, 20 pore-network realizations were generated and simulated to obtain the saturation distribution for the base case. For parametric studies, 10 pore-network realizations were used. The physical parameters for the present simulation are listed in Table 1. The domain size was $20 \times 20 \times 10$ and the GDL thickness L_z^0 was set to 200 μm.

The primary results from the pore-network simulation of the water transport in GDLs are presented in Fig. 7. The saturation distribution shown in Fig. 7(a) has a concave shape which was reported to be typical in invasion percolation processes [35,39,41,42]. In fact, the liquid water transport in GDLs belongs to the capillary fingering regime according to the phase diagram for drainage flows developed by Lenormand et al. [43]. The first breakthrough of liquid water occurs at about 30 s in Fig. 7(a), and the saturation level in GDLs continues to increase until the steady state is reached at about 120 s (see also Fig. 8 for the average saturation level). This transition in the saturation distribution after the first breakthrough is not generally observed in invasion percolation processes.

For a more detailed investigation, the flow rate of liquid water in the z-direction $Q_{w,z}$ normalized by the injection flow rate Q_{inj} is plotted in Fig. 7(b). Initially, $Q_{w,z}$ shows a highly non-uniform distribution along the z-direction, indicating that a considerable amount of liquid water flows in the x- and y-directions for the invasion percolation process. Even at the instance of the first breakthrough, $Q_{w,z}$ exiting the GDL is less than 5% of the injection flow rate Q_{inj}, suggesting that the invasion percolation process still prevails in

the water transport mechanism. However, $Q_{w,z}$ becomes uniform similar to Q_{inj} as the water transport approaches the steady state.

During the invasion percolation period, liquid water in a GDL flows randomly in every direction in search of possible paths for transport. Because most of the liquid water introduced to the GDL is used to invade pores in random directions, the flow rate of liquid water in the z-direction from the CL towards the GC is generally small. The transient invasion percolation period is characterized by the dynamic formation and motion of water/air interfaces. Once a network of pores invaded by liquid water is formed by the invasion percolation process, the transport of liquid water mainly occurs through the paths of the largest throat size. This steady state is characterized the static or time-stable water/air interfaces. The flow rate of water in the z-direction is the same as the injection flow rate introduced from the CL to the GDL at the steady state.
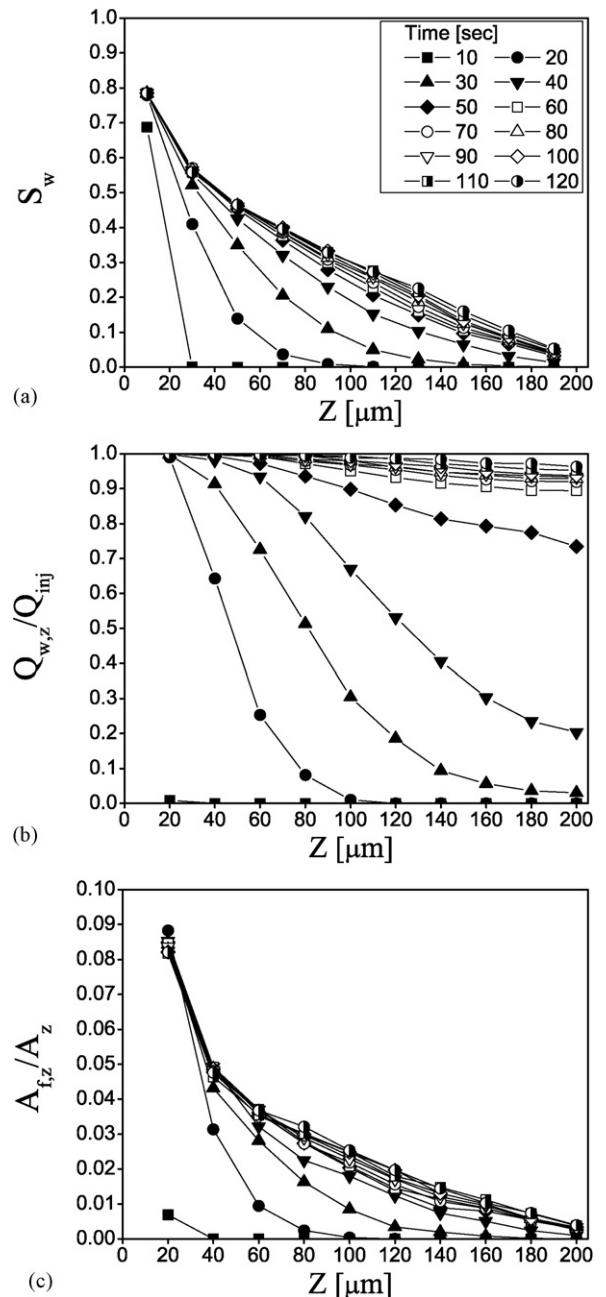

Fig. 7. The transient results of (a) the saturation distribution, (b) the normalized flow rate, and (c) the normalized flow area in a GDL.
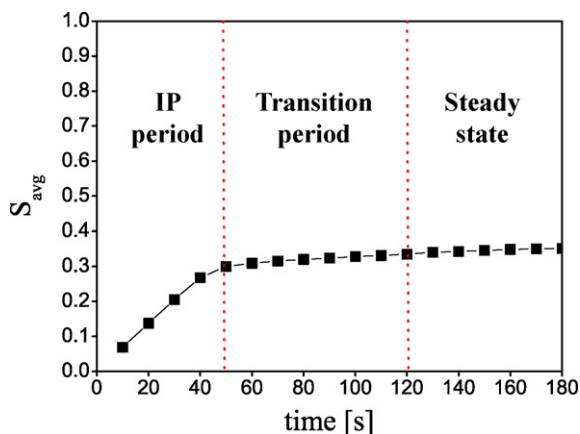
Fig. 8. The temporal evolution of the average saturation level in a GDL.

(a)

(b)

Fig. 10. The iso-surface plots for $S_w = 0.40$ at (a) $t = 30$ s and (b) $t = 120$ s.

The primary water transport paths in the steady state are a subset of the invaded pore network formed by the invasion percolation process. The ratio of the flow area $A_{f,z}$ to the total area A_z (the area of the calculation domain in the xy-plane) shown in Fig. 7(c) indicates that the water transport in the z-direction occurs through a small fraction of the available flow area. At steady state, the flow area $A_{f,z}$ at the mid-plane of the GDL ($z \approx 100\,\mu\text{m}$) is about 3% of the total area A_z, implying that only about 48 among the 400 (20×20) available throats in the z-direction are used for the water transport. Considering that the saturation at this position is about 0.3 as shown in Fig. 7(a), more than half of the invaded pores are dead-end pores which do not participate in the steady water transport in the z-direction.

The detailed transport behavior in the GDL at the steady state was investigated by inspecting the primary transport paths of liquid water as shown in Fig. 9. Lines connecting two adjacent pores were drawn when the calculated flow rate between the two pores were higher than the prescribed flow rates (1%, 5%, 15% and 25%). The darker and thicker lines denote higher flow rates in Fig. 9. The network of the primary transport paths shown in Fig. 9 is similar to the inverted tree-like structure proposed by Nam and Kaviany [10]. Paths with lower flow rates are more or less uniformly dispersed near the inlet boundary at the bottom. These paths converge into the paths with higher flow rates as liquid water flows
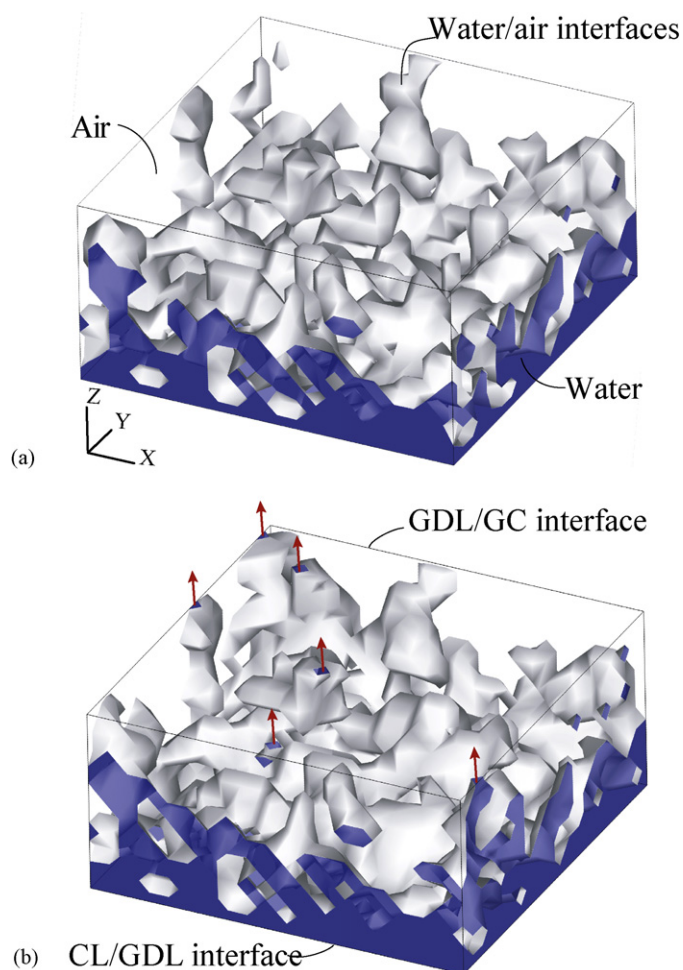
towards the GDL/GC interface. Finally, only six paths transport the entire injection flow rate out of the GDL. Fig. 9 also shows that the water transport by the steady two-phase flow occurs through rather straight paths near the GDL/GC interface.

Fig. 10 shows the iso-surfaces corresponding to $S_w = 0.40$. These iso-surfaces were constructed using the saturation distribution in pores while the presence of fibrous solid structure was ignored. These iso-surfaces are thought to approximately coincide with the water/air interfaces formed during the water transport in the GDL. The iso-surfaces at $t = 30$ s shown in Fig. 10(a) indicate that the rough water/air interfaces are formed by the capillary fingering process. The iso-surfaces at $t = 120$ s in Fig. 10(b) correspond to the steady state, where the location of six breakthrough pores in Fig. 9 can be clearly observed.

3.2. Parametric studies

3.2.1. Effect of the pore distortion

The effect of the pore distortion factor f on the water transport in GDLs is shown in Fig. 11. This parameter was introduced to consider the random distortion of the pore structure in GDLs. The pore distortion factor f modifies the pore-level P_c–S curves as shown in Fig. 4(a). Fig. 11(a) clearly indicates that the pores having smaller f easily build up the capillary pressure (magnitude) and thus export liquid water at lower saturation levels. Therefore, the steady saturation level for $f = 0.3$ is only about 65% of the saturation levels for $f = 0.7$ and 1. The saturation distribution at $t = 30$ s reveals that the
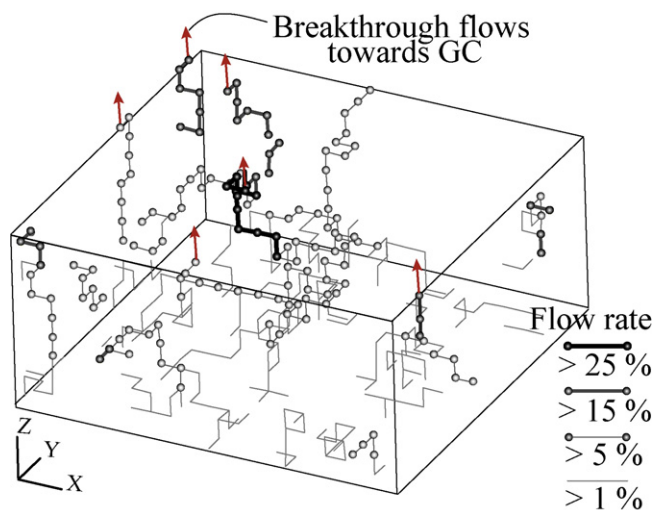

Fig. 9. The primary paths for liquid water transport in a GDL during the steady period.
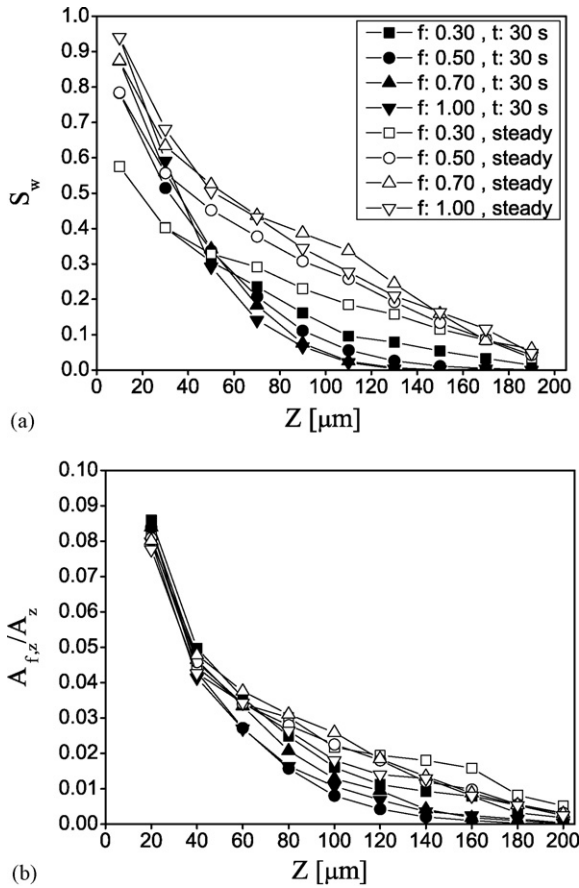
Fig. 11. The effect of the pore distortion factor f on (a) the saturation distribution and (b) the normalized flow area in GDLs.

water transport in GDLs quickly develops into a steady two-phase flow when f is small.

Fig. 11(b) shows that f has a minor impact on the flow area distribution at steady state, indicating that the two-phase flow pattern in GDLs is not significantly influenced by changing f. In fact, the two-phase flow pattern in a pore-network is more dependent on the topology of the pore-network than the pore-level capillary pressures in pores. Reducing f decreases the water saturation in each pore but hardly changes the flow pattern through the pore-network.

From these results, it can be inferred that the impact of variable pore distortion factors in pore-networks may not be critical; they can modify the saturation level in pores, but do not influence the flow pattern in pore-networks.

3.2.2. Effect of the compression of GDLs

The effect of the compression on the water transport in GDLs is presented in Fig. 12. The compressed pore-networks were generated by scaling the z-coordinate of all the lattice points in the randomized fiber lattices according to the compression ratio γ, defined as

$$\gamma = \frac{\bar{L}_z}{L_z^0}. \tag{18}$$

Here, L_z^0 is the original GDL thickness (200 μm) and $\bar{L}_z$ is the mean thickness of the compressed GDLs.

The compression ratio γ was varied as 1, 0.85, and 0.7, which corresponded to $\bar{L}_z$ of 200 μm, 170 μm, and 140 μm, respectively. The isotropic pore-networks ($\gamma = 1$) have the same throat size

in each direction. When the compression ratio decreases below 1, the throat size in the x- and y-directions (in-plane direction) becomes smaller than that in the z-direction (through-plane direction). For example, the hydraulic radius r_t of throats (without randomization) is estimated to be 5 μm for $\gamma = 1$, 4.12 μm for $\gamma = 0.85$, and 2.85 μm for $\gamma = 0.7$ in the in-plane direction. However, r_t is always 5 μm in the through-plane direction, irrespective of γ.

In Fig. 12(a), the predicted saturation distributions for $\gamma \geq 0.85$ have similar concave shapes which is typical for invasion percolation processes, but with a slightly shifted saturation level. However the saturation distribution for $\gamma = 0.7$ shows a rather linear shape at the steady state, indicating slight change in the flow pattern. The compressed GDLs have lower throat entry pressure in z-direction than those in the x- and y-directions. This hinders the random invasion of liquid water in the transverse direction (the x- and y-directions), resulting in the preferential invasion of liquid water in the z-direction. The flow area distribution shown in Fig. 12(b) also indicates that the flow in GDLs occurs preferentially in the z-direction as the compression ratio γ decreases. The transient saturation distribution at $t = 30$ s shows that the flow reaches the steady state more quickly for smaller compression ratio γ.

Note that only the effect of GDL compression on the throat geometry (change in the throat radius) was considered in the present simulation, while that on the pore geometry (e.g., change in the pore distortion factor) was ignored. Thus, further research might be required to more properly assess the effect of GDL compression.
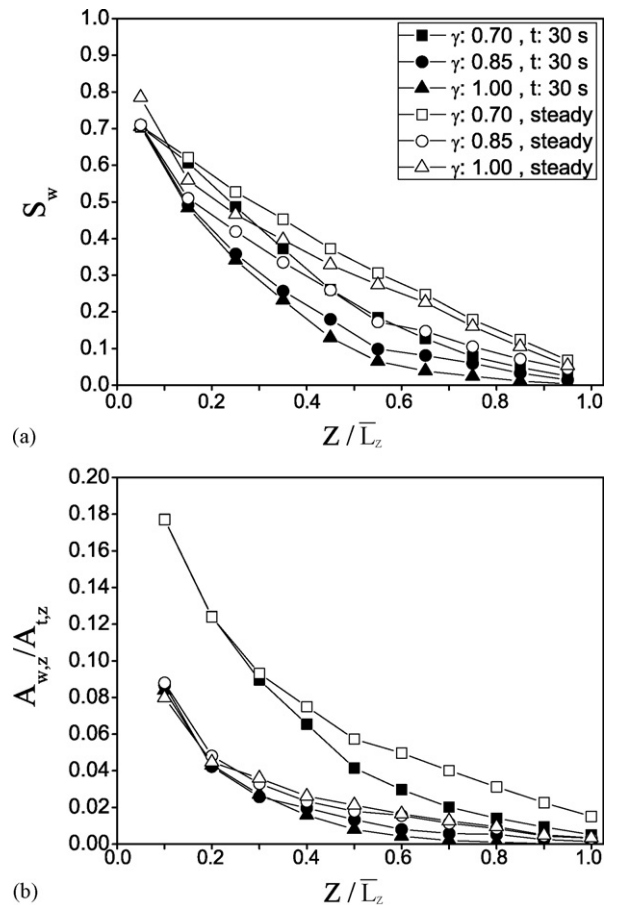

Fig. 12. The effect of the compression ratio γ on (a) the saturation distribution and (b) the normalized flow area in GDLs.
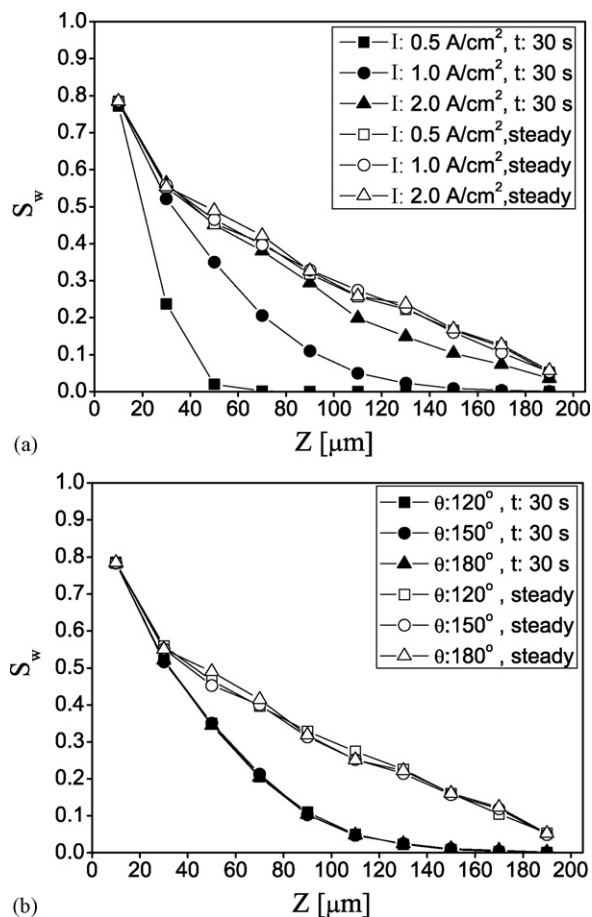
Fig. 13. The effect of (a) the current density I and (b) the contact angle θ_w on the saturation distribution in GDLs.

3.2.3. Effect of the flow rate and the hydrophobicity

The flow rate of liquid water in a cathode GDL is a function of the operating current density I. In this study, the uniform flux condition was imposed at the inlet boundary of the pore-networks as

$$\frac{Q_{inj}}{A_z} = \frac{M_{H_2O}}{\rho_{H_2O}} \frac{I}{2F}(1 + 2\alpha_{eff}), \tag{19}$$

where α_{eff} is the effective electro-osmosis drag coefficient, which was set to zero for simpler presentation of results. The uniform flux condition of Eq. (19) was implemented by imposing a constant source of liquid water $Q_{inj}/(N_x N_y)$ to each pore contacting the inlet boundary.

The influence of the flow rate was investigated in Fig. 13(a) by changing the current density I. Fig. 13(a) shows that the flow rate does not significantly affect the water transport in GDLs, although the time to reach a steady state decreases as the flow rate increases. The saturation distribution at $t = 30$ s indicates that the invasion percolation process is accelerated by a higher flow rate of water. However, the steady saturation distribution shows no meaningful change while I is increased four times from 0.5 to 2.0 A/cm². This is believed to be due to the fact that the water transport in GDLs is a strongly capillary-driven process. Further studies are under way to clarify the mechanism by which high current density leads to high saturation level within GDLs.

Fig. 13(b) shows the effect of the hydrophobicity of GDLs on the water transport. No noticeable difference is observed in the steady as well as the transient saturation distributions when the contact angle θ_w is changed. The actual effect of the contact angle

on the microscopic capillary phenomena is generally too complex to be accurately considered in numerical models. Thus, the effect of the contact angle is usually incorporated into the surface tension σ by multiplying with $\cos\theta_w$, such as the $\sigma\cos\theta_w$ terms in Eqs. (2) and (3). In this case, the two-phase flow pattern does not change when the contact angle is varied as shown in Fig. 13(b), though the capillary pressure level increases according to the magnitude of $\cos\theta_w$.

4. Discussion

The flow pattern of a two-phase drainage flow in porous media (a non-wetting fluid displaces a wetting fluid) is dependent on two dimensionless parameters. These are the viscosity ratio $M = \mu_{inv}/\mu_{dis}$ (the ratio of the viscosity of an invading fluid to that of a displaced fluid) and the capillary number $Ca = \mu_{inv}U/\sigma\cos\theta$ (the ratio of the viscous force to the capillary force). According to the magnitude of the two parameters, Lenormand et al. [43] classified the two-phase drainage flow into three regimes, i.e., the stable displacement, capillary fingering, and viscous fingering regimes. When the capillary number Ca is small due to slow displacement rate, non-wetting fluids preferentially invade the pores of lower capillary entry pressures, forming long and meandering paths (capillary fingering). When the viscosity ratio M is small, non-wetting fluids preferentially flow through the pores of lower viscous resistances, resulting in rather straight paths (viscous fingering). When both Ca and M are large, non-wetting fluids penetrate into porous media forming an approximately flat invasion front (piston-like stable displacement).

PEMFCs are generally operated at current densities below 2 A/cm². Under these operating conditions, the flow rate of liquid water through hydrophobic GDLs corresponds to the capillary number Ca of approximately 10^{-8} to 10^{-9}. Considering that the viscous ratio M of water to air is an order of 10, the two-phase flow in GDLs belongs to the capillary fingering regime according to Lenormand et al. [43]. The quasi-static displacement models for $Ca \approx 0$ predicted that the non-wetting phase saturation distribution in porous media maintains a concave shape along the flow direction with a constant fractal dimension [41]. Similar saturation distributions were predicted by the present analysis and also by Sinha and Wang [31]. These results indicate that the water transport in hydrophobic GDLs is dominated by the invasion percolation process to which conventional continuum flow models is difficult to be applied.

The saturation distribution presented in Sinha and Wang [31] showed a concave shape and the whole transport process reached a steady state shortly after the first breakthrough of liquid water was predicted. The present model also predicted similar saturation distribution in GDLs at the transient state, but showed longer transition period toward a higher saturation level in GDLs at the steady state. It should be noticed that several modeling aspects are different between the present pore-network model and that of Sinha and Wang [31]. First, all void volume was assigned to pores and throats were treated as volumeless passages between the pores (having entry pressures and viscous resistance). Second, the pore-level (microscopic) P_c–S correlations were explicitly included in the present model. However the difference in the modeling approaches cannot be the primary reason for the different steady saturation distributions. Instead, the discrepancy in the saturation distributions is believed to have been caused by the different inlet boundary conditions used to introduce liquid water into the pore-networks.

In most numerical and experimental studies on drainage processes [35,39,44] or the water transport in hydrophobic GDLs [13,45], a continuous non-wetting fluid was assumed to be pushed towards a porous material. This condition results in a spatially
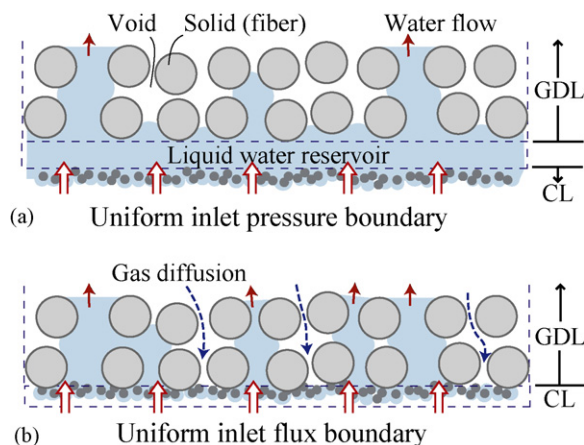
Fig. 14. Two possible boundary conditions for the liquid water entering GDLs: (a) a uniform inlet pressure condition and (b) a uniform inlet flux condition.

uniform pressure of the non-wetting fluid over the entire area of the inlet boundary (uniform inlet pressure condition). Thus, the non-wetting fluid preferentially intrudes larger pores in the porous material, resulting in a spatially non-uniform flux at the inlet surface. However, the uniform inlet pressure condition is less plausible in PEMFC operations. For example, Sinha and Wang [31] assumed that the inlet face of GDLs (between a CL and a GDL) is in contact with a liquid water reservoir as shown in Fig. 14(a). Even in the liquid water reservoir, uniform pressure at the inlet face of the GDL is difficult to be attained due to the viscous pressure drop. This liquid water reservoir can significantly hinder the diffusion of reactant gases towards the CL, resulting in the failure of PEMFCs. In addition, highly (spatially) non-uniform liquid water flux into GDLs resulted from the uniform inlet pressure condition seems to contradict rather uniform generation of liquid water in the CL. Thus, a spatially uniform inlet flux condition shown in Fig. 14(b) is believed to be a more plausible boundary condition for the liquid water entering the GDL.

The spatially uniform inlet flux condition results in the water transport behavior which is significantly different from the ordinary drainage flow with a spatially uniform inlet pressure condition. The flow rate of liquid water exiting a GDL is very small at the instance of the first breakthrough as shown in Fig. 6(b). This indicates that the liquid water delivered by that breakthrough path is only a small fraction of the liquid water introduced to the GDL. That flow rate upon the first breakthrough is correspondent to the liquid water introduced through a certain small area of the inlet boundary. At this moment, liquid water from the remaining inlet area is still invading pores by the invasion percolation process in search of the other breakthrough paths for its own. Subsequently, more and more breakthrough paths are formed and finally a steady state is reached. Therefore the uniform inlet flux condition is believed to be the primary cause for the increase of the saturation level in GDLs despite of their very small thickness.

Although the present results and those of Sinha and Wang [31] support the dominance of capillary processes in the water transport, whether the water transport in hydrophobic GDLs is driven by the invasion percolation (with capillary-dominant concave saturation distribution) or the continuum flow (with viscous-dominant convex saturation distribution) is still controversial. High-resolution neutron radiographic techniques were recently applied to probe the cross-sectional liquid water content in PEMFCs [46,47]. The measured water content distribution in GDLs was neither neatly concave nor completely convex, suggesting that more complex mechanisms might work in the water transport in GDLs

in addition to the invasion percolation and the continuum flow. This should be clarified by further studies based on numerical and experimental means.

5. Conclusion

The water transport in hydrophobic GDLs of PEMFCs was studied using a pore-network model that considered the microscale behavior of liquid water in pores and through throats. The pore-network analysis showed that the water saturation distribution in GDLs has a concave shape along the flow direction, which indicates that the invasion percolation process is an important transport mechanism. The uniform inlet flux condition was suggested as a proper boundary condition for the liquid water entering GDLs, which contributed to the rather higher saturation level in GDLs.

Several geometrical and capillary properties of GDLs were varied to investigate their influences on the water transport behaviors. Reducing the pore distortion factor f decreased the overall saturation level but did not significantly change the two-phase flow pattern in GDLs. When the compression ratio γ was decreased, the saturation distribution became rather linear due to change in the flow pattern. The current density I and the contact angle θ_w did not significantly affect the water saturation in GDLs in the present simulations.

Acknowledgement

Appendix A

The dimensionless resistance factor β accounts for the lowered conductance of a wetting fluid (air) which flows along the sharp corners of a noncircular throat. According to [37–39], β is calculated as

$$\beta = \frac{12 \sin^2\alpha(1-B)^2(\psi_1 - B\psi_2)(\psi_3 + f_i B\psi_2)^2}{(1-\sin\alpha)^2 B^2(\psi_1 - B\psi_2)^3}, \tag{A1}$$

$$\psi_1 = \cos^2(\alpha + \theta_a) + \cos(\alpha + \theta_a)\sin(\alpha + \theta_a)\tan\alpha, \tag{A2}$$

$$\psi_2 = 1 - \frac{\theta_a}{\pi/2 - \alpha}, \tag{A3}$$

$$\psi_3 = \frac{\cos(\alpha + \theta_a)}{\cos\alpha}, \tag{A4}$$

$$B = \left(\frac{\pi}{2} - \alpha\right)\tan\alpha. \tag{A5}$$

Here, α is the half angle of the corners ($\pi/4$ for rectangular throats), θ_a is the contact angle of air ($\theta_a = \pi - \theta_w$), and f_i is a factor depending on the boundary condition at the water/air interface ($f_i = 1$ for a no-slip boundary).

References

[1] J.J. Baschuk, X. Li, J. Power Sources 86 (2000) 181.
[2] K. Tüber, D. Pocza, C. Hebling, J. Power Sources 124 (2003) 403.
[3] X.G. Yang, F.Y. Zhang, A.L. Lubawy, C.Y. Wang, Electrochem. Solid St. 7 (2004) A408.
[4] A. Theodorakakos, T. Ous, M. Gavaises, J.M. Nouri, N. Nikolopoulos, H. Yanagihara, J. Colloid Interf. Sci. 300 (2006) 673.
[5] D. Spernjak, A.K. Prasad, S.G. Advani, J. Power Sources 170 (2007) 334.
[6] T. Ous, C. Arcoumanis, J. Power Sources 173 (2007) 137.
[7] S. Dutta, S. Shimpalee, J.W. Van Zee, J. Appl. Electrochem. 30 (2000) 135.
[8] A. Golpaygan, N. Ashgriz, Int. J. Energy Res. 29 (2005) 1027.
[9] K. Jiao, B. Zhou, P. Quan, J. Power Sources 157 (2006) 226.
[10] J.H. Nam, M. Kaviany, Int. J. Heat Mass Transfer 46 (2003) 4595.
[11] H.M. Yu, J.O. Schumacher, M. Zobel, C. Hebling, J. Power Sources 145 (2005) 216.

[12] H.M. Yu, C. Ziegler, M. Oszcipok, M. Zobel, C. Hebling, Electrochim. Acta 51 (2006) 1199.
[13] S. Litster, D. Sinton, N. Djilali, J. Power Sources 154 (2006) 95.
[14] N. Djilali, Energy 32 (2007) 269.
[15] W. He, G. Lin, T.V. Nguyen, AIChE J. 49 (2003) 3221.
[16] Q. Dong, J. Kull, M.M. Mench, J. Power Sources 139 (2005) 106.
[17] E. Stumper, M. Lohr, S. Hamada, J. Power Sources 143 (2005) 150.
[18] R. Satija, D.L. Jacobson, M. Arif, S.A. Werner, J. Power Sources 129 (2004) 238.
[19] N. Pekula, K. Heller, P.A. Chuang, A. Turhan, M.M. Mench, J.S. Brenizer, K. Unlu, Nucl. Instrum. Methods Phys. Res. A 542 (2005) 134.
[20] D. Natarajan, T.V. Nguyen, J. Electrochem. Soc. 148 (2001) 1324.
[21] L.X. You, H.T. Liu, Int. J. Heat Mass Transfer 45 (2002) 2277.
[22] T. Berning, N. Djilali, J. Electrochem. Soc. 150 (2003) A1589.
[23] D. Natarajan, T.V. Nguyen, J. Power Sources 115 (2003) 66.
[24] H. Sun, H. Liu, L.J. Guo, J. Power Sources 143 (2005) 123.
[25] A.Z. Weber, J. Newman, J. Electrochem. Soc. 152 (2005) A677.
[26] C. Ziegler, H.M. Yu, J.O. Schumacher, J. Electrochem. Soc. 152 (2005) A1555.
[27] U. Pasaogullari, C.Y. Wang, K.S. Chen, J. Electrochem. Soc. 152 (2005) A1574.
[28] J.T. Gostick, M.W. Fowler, M.A. Ioannidis, M.D. Pritzker, Y.M. Volfkovich, A. Sakars, J. Power Sources 156 (2006) 375.
[29] B. Markicevic, A. Bazylak, N. Djilali, J. Power Sources 171 (2007) 706.
[30] J.T. Gostick, M.A. Ioannidis, M.W. Fowler, M.D. Pritzker, J. Power Sources 173 (2007) 277.

[31] P.K. Sinha, C.Y. Wang, Electrochim. Acta 52 (2007) 7936.
[32] M. Karviany, Principles of Heat Transfer in Porous Media, second ed., Springer, New York, 1999.
[33] J.G. Pharoah, K. Karan, W. Sun, J. Power Sources 161 (2006) 214.
[34] J.T. Gostick, M.W. Fowler, M.D. Pritzker, M.A. Ioannidis, L.M. Behra, J. Power Sources 162 (2006) 228.
[35] K.E. Thompson, AIChE J. 48 (2002) 1369.
[36] S. Ma, G. Mason, N.R. Morrow, Colloid Surface A 117 (1996) 273.
[37] D. Zhou, M. Blunt, F.M. Orr, J. Colloid Interf. Sci. 187 (1997) 11.
[38] R.G. Hughes, M.J. Blunt, Adv. Water Res. 24 (2001) 409.
[39] M. Singh, K.K. Mohanty, Chem. Eng. Sci. 58 (2003) 1.
[40] K. Aziz, A. Settari, Petroleum Reservoir Simulation, Applied Science Publishers, London, 1979.
[41] M. Ferer, G.S. Bromhal, D.H. Smith, Physica A 311 (2002) 5.
[42] M. Ferer, G.S. Bromhal, D.H. Smith, Physica A 319 (2003) 11.
[43] R. Lenormand, E. Touboul, C. Zarcone, J. Fluid Mech. 189 (1988) 165.
[44] I. Neuweiler, I. Sorensen, W. Kinzelbach, Adv. Water Resour. 27 (2004) 1217.
[45] J. Benziger, J. Nehlsen, D. Blackwell, T. Brennan, J. Itescu, J. Membr. Sci. 261 (2005) 98.
[46] M.A. Hickner, N.P. Siegel, K.S. Chen, D.S. Hussey, D.L. Jacobson, M. Arif, J. Electrochem. Soc. 155 (2008) B427.
[47] C. Hartnig, I. Manke, R. Kuhn, N. Kardjilov, J. Banhart, W. Lehnert, Appl. Phys. Lett. 92 (2008) 134106.